Fluidization Regimes of Dense Suspensions of Geldart Group A Fluidized Particles in a High Aspect Ratio Column

Ronny Gueguen, Guillaume Sahuquet, Samuel Mer, Adrien Toutant, Françoise Bataille, Gilles Flamant

Chemical Engineering Science 267 (2023) 118360

Contents lists available at ScienceDirect

Chemical Engineering Science

journal homepage: www.elsevier.com/locate/ces

Fluidization regimes of dense suspensions of Geldart group A fluidized particles in a high aspect ratio column

Ronny Gueguen [a], Guillaume Sahuquet [a], Samuel Mer [b], Adrien Toutant [b], Françoise Bataille [b], Gilles Flamant [a,*]

[a] Processes, Materials and Solar Energy Laboratory, PROMES-CNRS, 7 Rue du Four Solaire, 66120 Font-Romeu, France
[b] Processes, Materials and Solar Energy Laboratory, PROMES-CNRS, University of Perpignan (UPVD), Tecnosud, Rambla de la Thermodynamique, 66100 Perpignan, France

HIGHLIGHTS

- Particle-driven receiver involves fluidization in tubes with high aspect ratio.
- Fluidization regimes result from both overpressure and secondary air flow.
- The local slip velocity governs the fluidization regimes and their transitions.
- Regime transitions differ from the one previously observed in risers.

GRAPHICAL ABSTRACT

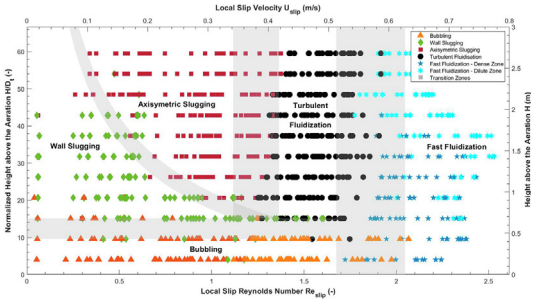

ARTICLE INFO

Article history:
Received 29 July 2022
Received in revised form 28 October 2022
Accepted 25 November 2022
Available online 28 November 2022

Keywords:
Tubular particle solar receiver
Particle-driven CSP
Fluidization regimes
Particle circulation
Fluidization diagram
Slip velocity

ABSTRACT

Fluidization regimes were studied in numerous papers with applications in risers in which gas velocity is the main driving force. The situation is different when a tube is immersed in a fluidized bed vessel in which a pressure is imposed to move the particle upward. The particle-in-tube solar receiver concept is based on this latter operation mode with the aim to heat particles at high temperature with concentrated solar energy. This study identifies the fluidization regimes in a pressure-driven system that includes a secondary aeration to control the air velocity in the tube. Bubbling, slugging, turbulent and fast fluidization regimes are determined thanks to temporal pressure signal processing methods and a regime map is plotted. The transition velocities are significantly lower than in classical risers. The local slip velocity is defined as the governing parameter of the flow structure and the variation of the local particle volume fraction is discussed.

1. Introduction

1.1. Particles as heat transfer medium

Concentrated solar technology can produce clean and dispatchable power and thus contribute solving the global climate change issue. Indeed, solar thermal energy offers the possibility to produce electricity on demand from an unlimited resource when coupled with a heat storage. In concentrated solar power plants, in particular for solar power towers, the solar radiation is focused thanks to a heliostat field toward a receiver located at the top of a tower, in which a heat transfer fluid is circulating. This heat transfer fluid can be stored and then used in the energy conversion process, or directly brought into a heat exchanger to heat a working fluid that powers a turbine.

Several heat transfer fluids are used in commercial concentrated solar plants depending on the desired temperatures and

* Corresponding author.
E-mail address: Gilles.Flamant@promes.cnrs.fr (G. Flamant).

https://doi.org/10.1016/j.ces.2022.118360
0009-2509/

Nomenclature

d_X	Diameter corresponding to the X % value on the cumulated particle size distribution (μm)
d_{SV}	Sauter diameter of the powder sample (μm)
d_V	Volume diameter of the powder sample (μm)
D_t	Internal diameter of the tube (m)
G_p	Particle mass flux ($kg.m^{-2}.s^{-1}$)
h_s	Transition height from bubbles to established slugs (m)
H_{bed}	Height of the suspension in the tube (m)
H_t	Height of the tube (m)
$\dot{m}_p$	Particle mass flow rate ($kg.s^{-1}$)
P_i	Relative pressure in the tube at the level of the i^{th} pressure socket (mbar)
P_{sky}	Freeboard pressure in the dispenser (mbar)
P_{tot}	Total relative pressure in the dispenser (mbar)
$\dot{q_{ae}}$	Aeration flow rate ($m^3.h^{-1}$)
Re_{slip}	Particular Reynolds number relative to the slip velocity (–)
S_t	Internal section of the tube (m^2)
U_{air}	Superficial air velocity in the tube ($m.s^{-1}$)
U_k	Fast fluidization velocity ($m.s^{-1}$)
U_{mb}	Minimum bubbling velocity ($m.s^{-1}$)
U_{mf}	Minimum fluidization velocity ($m.s^{-1}$)
U_{slip}	Slip velocity between the air and the particle ($m.s^{-1}$)
U_t	Turbulent fluidization velocity ($m.s^{-1}$)
α_h	Overall particle volume fraction in the tube (–)
α_i	Local particle volume fraction in the tube (–)
α_{bulk}	Particle volume fraction of the fixed bed (–)
ΔH	Distance between two pressure sockets (m)
ΔP_{acc}	Pressure drop due to the particles acceleration (mbar)
ΔP_{bed}	Pressure drop through the fluidized bed in the dispenser (mbar)
ΔP_i	Differential pressure in the tube between two pressure sockets (mbar)
μ_{air}	Dynamic viscosity of the air ($kg.m^{-1}.s^{-1}$)
ρ_p	Bulk density of the particle sample ($kg.m^{-3}$)

the concentration technology (Benoit et al., 2016). In solar towers, the most commonly used heat transfer fluid is molten salt. The molten salt operation temperatures range between 220 and 565 °C to avoid solidification and decomposition, respectively. The lower limit involves a constant energy consumption to maintain the salt temperature above the melting point, while the upper limit is a security constraint linked to the nitrate salt decomposition (Zhang et al., 2017).

In order to increase the global efficiency of the power plant, several high-efficiency thermodynamic cycles are under development, such as combined or supercritical cycles (Dunham and Iverson, 2014). These cycles need high working temperature, above 650 °C, which thus requires the change of the heat transfer fluid. One of the possible options consists in using solid particles because they are suitable for operating as both heat transfer and storage media. This option eliminates high-pressure constraints, enables high working temperatures (of 1000 °C and even more) and leads to low-cost thermal energy storage (Jacob et al., 2016).

Three main technologies of solar receiver using particles are under development. In the falling particle and the centrifugal receivers, designed respectively by the Sandia National Laboratory (USA) and the German Aerospace Center (Germany), the particles are directly irradiated by the concentrated solar flux (Ho et al., 2017; Wu et al., 2014). The PROMES laboratory of the National Center for Scientific Research (CNRS, France) develops since 2010 with partners a concept of solar receiver based on the circulation of fluidized particles (Flamant et al., 2010). In this concept, named "particle-in-tube receiver" or "Upward Bubbling Fluidized Bed", the particles are fluidized in a vessel fluidized bed called "the dispenser". The vertical irradiated tubes are immersed in the fluidized bed, and an upward forced circulation is set up by controlling the overpressure in the dispenser. The particles are thus indirectly heated by the tube's walls, which is similar to the molten salt receiver technology. A secondary air flow rate called "aeration" is injected at the bottom of the tubes to stabilize the particle flow. Several experimental and numerical studies have been carried out with the particle-in-tube solar receiver under the European projects CSP2 and Next-CSP (https://cordis.europa.eu/project/id/282932; Next-CSP, 2020). Particles that belong to the group A of the Geldart's classification have been selected (Geldart, 1973). Outlet particles temperatures and wall-to-particles heat transfer coefficients above respectively 700 °C and 1000 W/m^2K have been determined experimentally and numerically, largely proving the interest of the concept (Flamant et al., 2013; Benoit et al., 2015; Perez-Lopez et al., 2016; Boissiere et al., 2015; Le Gal et al., 2019; Ansart et al., 2017; Benoit et al., 2018; Kong et al., 2017; Sabatier et al., 2020; Deng et al., 2021). However, in such a gas-particle flow, several fluidization regimes can occur in the receiver tubes depending on the operating conditions. The regimes result in various particle volume fraction and particle mixing, thus various heat transfer rates (Kunii and Levenspiel, 1991). Therefore, it is necessary to establish a link between the operating conditions and the fluidization regimes in order to improve the performance of the solar receiver. Nonetheless, the suspension behavior was not thoroughly analyzed in the earlier cited studies because of their insufficient number of pressure probes.

1.2. Fluidization regimes in classical columns

In classical fluidization columns, the air injection at the bottom of the column enables the particles fluidization. Several fluidization regimes occur depending on the air velocity, the column geometry and the particles properties (Kunii and Levenspiel, 1991).

The minimum fluidization velocity is the gas velocity that delimitates the transition between the fixed bed and the fluidized bed, where the particles acquire the properties of a quasi-fluid (Kunii and Levenspiel, 1991). Increasing the gas velocity for group A particles of the Geldart's classification results in a dense and homogenous fluidized bed, without any bubble until the minimum bubbling velocity, at which the first bubble erupts at the bed surface (Abrahamsen and Geldart, 1980). Bubbles are then coalescing with the height until they reach a maximum bubble size (Geldart, 1973). Either at higher gas velocity or if the bubble size reaches approximately 60 % of the column diameter, bubbles are merging into slugs (Kong et al., 2017). The consequence of the slugging regime – large and slow bubbles – is the decrease of both the mean particle volume fraction and the particle mixing. In wall-heating conditions, it is associated with a decrease of the wall-to-fluidized bed heat transfer coefficient (Deng et al., 2021).

Increasing the gas velocity results in the appearance of the turbulent fluidization when the bubble coalescence becomes compensated by their scission (Yerushalmi and Cankurt, 1979). Disordered

gas structures – vortices – appear in the bed, resulting in a less defined upper surface of the fluidized bed. In this regime, the gas-particle suspension is still relatively dense and the particle mixing is vigorous, thus leading to a high heat transfer rate (Bi et al., 2000).

The fast fluidization regime occurs when the gas velocity reaches the particle terminal velocity (Grace et al., 2020). In this regime, the particles are entrained outside of the column as clusters (Grace et al., 2020). The commonly used Circulating Fluidized Bed – involving risers – are generally working in the fast fluidization regime that results in strong particle mixing but low mean particle volume fraction.

Fluidization regimes in risers have been widely studied in the literature, and several attempts to establish regimes diagrams have been published (Yerushalmi and Cankurt, 1979; Grace et al., 2020; Rabinovich and Kalman, 2011; Geldart and Chap, 1986; Bi and Grace, 1995). Nonetheless, the establishment of the particle circulation differs in the fluidized particle-in-tube solar receiver concept studied in this paper. Actually, in the latter, the upward flow of the gas-particle suspension is the result of the combination of both the air velocity and the overpressure in the dispenser, while in risers, it is commonly generated by applying a high gas velocity at the bottom of the tube (Hafizur Rahman et al., 2020; Breault et al., 2020). Moreover, riser diameters are larger than solar receiver tubes and their tube aspect ratios are smaller (typically around 10) (Stefanova et al., 2011). The original characteristics of fluidized particle-in-tube solar receiver concept offer the opportunity to maintain a dense suspension, i.e. a relatively high particle volume fraction, and consequently to reach a high wall-to-bed heat transfer rate.

1.3. Objectives

In the previous cited studies about the fluidized particle-in-tube receiver (Flamant et al., 2013; Benoit et al., 2015; Perez-Lopez et al., 2016; Boissiere et al., 2015; Le Gal et al., 2019; Ansart et al., 2017; Benoit et al., 2018; Kong et al., 2017; Sabatier et al., 2020; Deng et al., 2021), the superficial air velocities in the tube were limited to a maximum of 0.30 m/s, in order to reduce the formation of slugs. A concept of "Bubble Rupture Promoter (BRP)" within the tube has been tested, aiming to prevent slugs' formation (Deng et al., 2021). The main idea behind this solution is creating turbulent fluidization inside the space limited by the BRP, but such inserts integrated in an industrial-scale solar receiver are expected to be expensive regarding the number of tubes and their heights (Gueguen et al., 2020). This approach may be applied in the bare tubes (without insert) of the fluidized particle-in-tube concept by increasing the air velocity, to reach the conditions of the turbulent fluidization regime (Grace et al., 2020).

In a previous work, tests in specific conditions – without particle circulation, and with particle mass fluxes of 50 and 100 kg/(m^2.s) – have been precisely analyzed, proving that the fluidization regimes encountered in the tube are similar to those encountered in risers (Gueguen et al., 2021). The turbulent and fast fluidization regimes have been observed thanks to the increase of the air velocity up to 0.54 m/s. Furthermore, it shown that the identification of the regimes is possible using a non-intrusive method, i.e. by analyzing the pressure evolution with different signal processing methods. More extensive data are presented in this paper.

The present research is an original experimental contribution to the analysis of fluidization regimes inside a tube characterized by a high aspect ratio (height over diameter >70), at ambient temperature. It extends our earlier study (Gueguen et al., 2021) – where classical fluidization regimes have been observed – in establishing a precise fluidization regime diagram while specifying their transitions velocities. The experimental set-up is first presented (particles used, description of the cold rig and presentation of the pressure signals processing methods), followed by the evolution of the particle flow characteristics – particle flow rate, particle volume fraction and fluidization regime – as functions of the operating parameters. It then leads to the establishment of a fluidization regimes diagram accounting for all test results. Finally, a discussion on the regime's detection criteria is proposed.

2. Experimental set-up

2.1. Particles

Olivine particles have been selected as heat transfer medium in the framework of the Next CSP European project because they offer attractive thermomechanical, health and cost characteristics (Next-CSP, 2020; Kang et al., 2019). The fluidization properties of the olivine particles are presented in Table 1. They have been experimentally measured and more detailed in (Gueguen et al., 2021).

The various diameters that characterize the particle size distribution have been determined by laser diffraction, using a Malvern Mastersizer 3000 granulometer. The Sauter mean diameter d_{SV} is estimated at 61 µm, slightly lower than the median diameter d_{50} because of fine particles in the sample (Geldart, 1986; Dodds and Baluais, 1993). Combined with the bulk density ρ_p of the powders, it confirms that it belongs to the group A of the Geldart classification (Geldart, 1973).

The particle volume fraction for the packed bed, α_{bulk}, was estimated at 0.48 by weighing a known particle volume. The minimum velocities of the various fluidization regimes have been experimentally measured in a 0.09 m I.D. (Internal Diameter) fluidization column, using the classic pressure drop versus the air velocity method. The minimum fluidization velocity, U_{mf}, was determined at the intersection of the curves relative to the fixed and fluidized beds, at decreasing air velocity (Kunii and Levenspiel, 1991). The minimum bubbling velocity, U_{mb}, was noticed when the first bubble erupts at the bed surface. It was identified in the pressure drop versus air velocity evolution by a brusque decrease (Abrahamsen and Geldart, 1980). Experimental values of U_{mf} and U_{mb} are in good agreement with the correlations generally used for group A particles (Grace et al., 2020; Wu and Baeyens, 1991).

At higher air velocities, the turbulent fluidization regime (U_t) is related to the maximum of the pressure fluctuations (Bi et al., 2000). In the scientific literature, it may be reported as the chocking velocity. But as discussed in (Bi et al., 1993), several chocking velocities have been introduced with different definitions. To avoid any confusion, the limit of the turbulent fluidization regime is named U_t in the present paper. The fast fluidization regime is noticed when the particles are entrained outside of the column. The bed is emptying, and it is identified by a permanent decrease of the pressure drop. The corresponding velocity is the particle terminal velocity, named U_k. The latter is characterized by a strong decrease of the pressure drop in a column without particle circulation (Bi et al., 2000; Rabinovich and Kalman, 2011).

2.2. Cold mock-Up description

A schematic description of the one-tube mock-up and its instrumentation is presented in Fig. 1. The olivine particles are fluidized in a 0.57 m^2 vessel, called the "dispenser", thanks to a constant air flow rate of 16.5 sm^3/h through a sintered porous bronze plate distributor. It corresponds to a superficial air velocity of 0.97 cm/s, i.e. 1.7 times the minimum bubbling velocity of the particles. A glass tube of 3.63 m total height and 45 mm internal diameter (D_t) –

Table 1
Thermal, physical and fluidization properties of the olivine sample.

Thermal and Physical Properties							Fluidization Threshold Air Velocities			
d_{10}(μm)	d_{50}(μm)	d_{90}(μm)	d_{SV}(μm)	d_V(μm)	ρ_p(kg/m^3)	α_{bulk}	Minimum of Fluidization, U_{mf} (cm/s)	Minimum of Bubbling, U_{mb} (cm/s)	Incipient Turbulent Fluidization, U_t (m/s)	Incipient Fast Fluidization, U_k (m/s)
39	70	124	61	81	3300	0.48	0.42	0.57	0.40	0.49

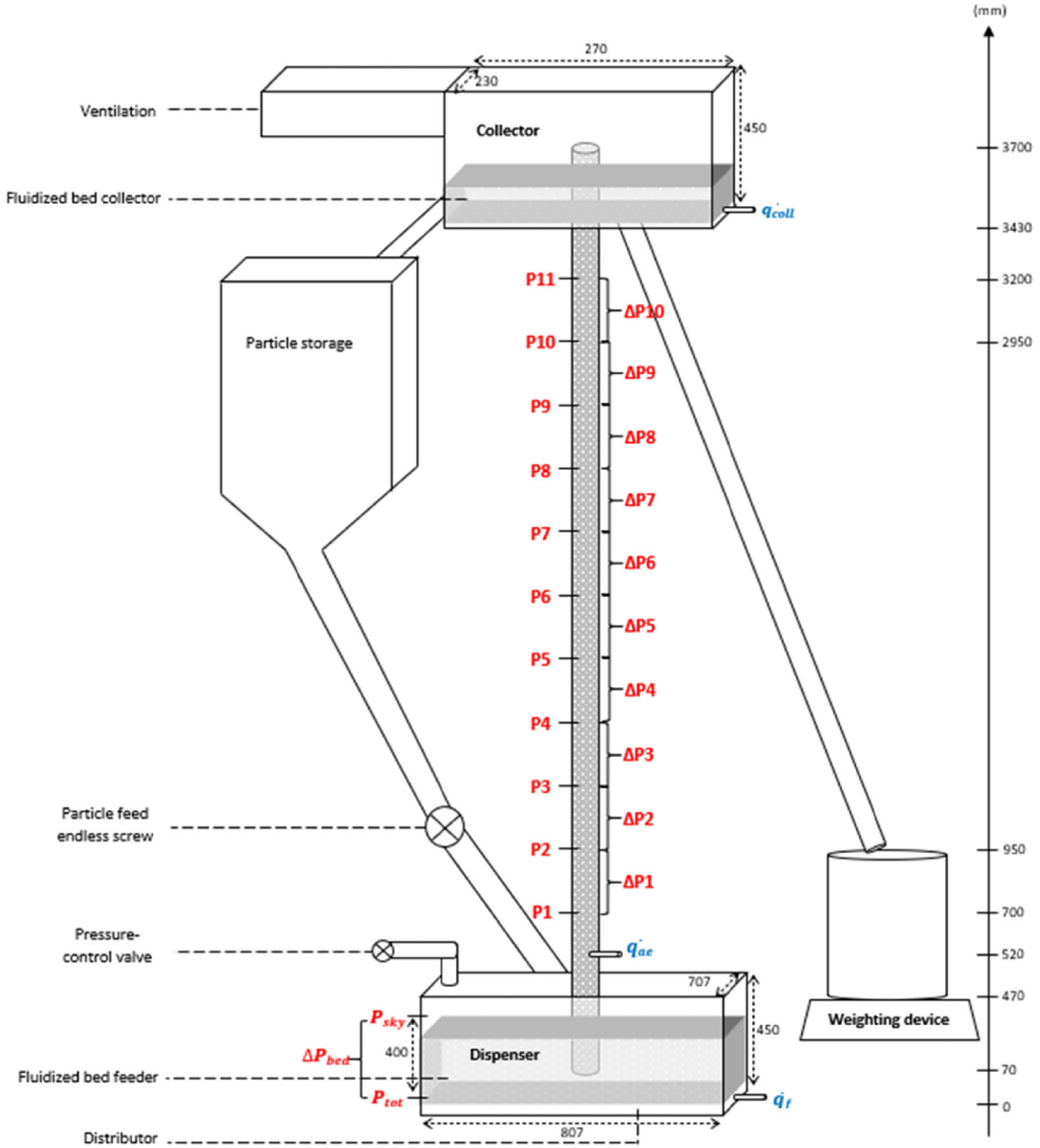

Fig. 1. Schematic description of the mock-up and its instrumentation (Gueguen et al., 2021).

i.e. an internal section S_t of 1.6 × 10^{-3} m^2 – is plunged in the fluidized bed up to 7 cm above the distributor. The upper part of the tube ends in a collector at atmospheric pressure in which particles are also fluidized. A secondary airflow, called "aeration", is injected at 0.45 m above the tube inlet at an airflow rate $\dot{q_{ae}}$ through a 1.5 mm I.D. nozzle to stabilize the suspension (Boissiere et al., 2015). The aeration is also used to control the fluidization regimes. The position of the nozzle is considered as the reference height for the rest of the study.

A leak valve is implemented at the top of the dispenser to control the freeboard pressure, P_{sky}. Closing the valve results in an increase of the pressure, leading to the gas-particle suspension flowing upward in the tube. The difference between the pressure in the dispenser, $P_{tot} = P_{sky} + \Delta P_{bed}$, and the atmospheric pressure,

is the driving force of the system, with ΔP_{bed} the pressure drop through the fluidized bed.

When the suspension reaches the collector, the particles flow outside of the tube in a tank placed on a weighing scale. The data are recorded at a frequency of 1 Hz with a precision of 0.01 kg, and the particle mass flow rate $\dot{m}_p$ is calculated by linear regression of the particles flowing in the tank. As a particle flow leads to a decrease of the amount of particles in the dispenser (controlled by the pressure drop ΔP_{bed}), the dispenser is fed from a storage tank thanks to a rotary valve to keep the pressure in the dispenser approximately constant during a test.

Eleven pressure sockets are implemented along the tube height each 0.25 m, the first one being located at 0.18 m above the aeration injector. They are connected to relative and differential pressure sensors as illustrated in Fig. 1, themselves connected to an acquisition system. The relative sensors (Siemens brand, model 7MF1641) having a small response time (5 ms) and an accuracy of 3 mbar, they are used for the analysis of flow dynamics with an acquisition frequency of 20 Hz. The differential sensors (Rosemont brand, model 2051C) have a long response time but high accuracy (0.05 mbar error), hence they are used to measure the particle volume fraction with high precision, with an acquisition frequency of 4 Hz. In order to prevent any particle entering inside the sensors, the sockets are equipped with sintered porous plates.

The data are recorded with acquisitions systems (National Instruments USB-6218 and Graphtec Midi Logger GL840) that fit the experimental requirements, connected to the Labview software. The pressure signals are analyzed thanks to several methods presented in the following section.

2.3. Identification and characteristics of the fluidization regimes

Several methods have been developed in the literature to identify and characterize the fluidization regimes, for example using acoustic measurement (Li et al., 2011), or thanks to pressure signal analyses (Stefanova et al., 2020; Chen et al., 2015; Vaidheeswaran et al., 2022; van der Schaaf et al., 2002; Johnsson et al., 2000; Fan et al., 1983). The latter are often used since it is a non-invasive method that enables relevant results even at elevated temperature. Then, as explained in the Introduction section, an earlier work shown that identifying the fluidization regimes in this concept of receiver is possible by using and combining temporal pressure signals processing methods (Gueguen et al., 2021). Firstly, the coherence analysis was used, in the frequency domain (van der Schaaf et al., 2002). The shape of the spectra, and both the frequencies and the magnitudes of the dominant peaks are characteristics of the regimes. Secondly, the cross-correlation function between two pressure signals was calculated, in the time domain (Johnsson et al., 2000). Here, both the shape of the function and the value of the maximum are relevant, the latter being related to the upward velocity of the perturbation (bubble, slug, cluster) (Fan et al., 1983). Thirdly, the relative pressure fluctuations and the shape of the particle fraction versus height trends were also pertinent indicators of the fluidization regime (Gueguen et al., 2021). The observed fluidization regimes and their characteristics are summarized below.

Classically, the acquisition times are of the order of the hour for pressure signals analyses in fluidized beds. Actually, most of the studies in the scientific literature is related to works without particle circulation, or in closed loops. The signals can be hence recorded at high acquisition frequencies to divide them into a high number of groups and to average the associated spectra for smoothing the data (van der Schaaf et al., 2002; Johnsson et al., 2000). In the present study, the acquisition time is limited during experiments in the particle circulation mode due to the capacity of the storage tank, because the system works in open loop. A high acquisition frequency would just lead to considerable noise in the spectra. The identification of the fluidization regimes is nonetheless possible by combining the different analysis methods, with pressure measurements recorded at 10 Hz for 205 s, to divide the signals in 4 groups of 1024 points each (Gueguen et al., 2021).

The exploding bubbling regime in the dispenser and the single bubbling regime identified at the bottom of the tube present the same characteristics. At low air velocities, but above the minimum bubbling velocity, these regimes are characterized by small bubbles at relatively high frequencies, with several peaks in the distributions at frequencies larger than 1 Hz and with very low magnitudes (van der Schaaf et al., 2002). As bubbles cause small pressure fluctuations, they are not detectable with the cross-correlation. The bubbles are coalescing with the tube height, until they are impacted by the walls and merge into slugs (Kong et al., 2017). The established slugging regime is axisymmetric, where the slugs are slow. On the spectra, slugs are characterized by a shift of the peak's distributions to the low frequencies, below 1 Hz. The associated pressure fluctuation magnitudes are still low but higher than for the bubbling regime. The latter increases with the increase of the air velocity. The cross-correlation function presents a maximum that enables calculating the upward slug velocity, which is in good agreement with the two-phase flow theory (Fan et al., 1983). Before the establishment of the axisymmetric slugging regime, bubbles are progressively merging into intermediate wall slugs, as shown by (Sabatier et al., 2020), where the bubbles are flowing along the tube walls. There is a coexistence of bubbles and slugs in this regime, and the spectra present the characteristics of both regimes.

At air velocities higher than U_t, the coalescence is compensated by the scission of the bubbles. It results in a transition to the turbulent fluidization regime with tube height (Bi et al., 2000). The latter is characterized in the spectra by peak distributions below 1 Hz associated with high magnitudes. Velocities are measurable with the cross-correlation function, and are higher than the upward slug velocities calculated with the two-phase theory.

The last regime identified is the fast fluidization, for air velocities higher than U_k. It corresponds to the entrainment of the particles in the fluidization column that induces a separation of the bed into a dense zone and a more dilute zone (Grace et al., 2020). At the bottom of the column, the relatively dense zone is associated to strong pressure fluctuations, and the particle fraction is lower than in the previous regimes. This regime is characterized in the spectra by low frequency peak distributions and very high magnitudes, higher than measured in the previous regimes. Along the tube height, a more dilute zone follows this bottom zone, where the particles are entrained outside of the tube. This entrainment is due to the formation of particles clusters (Grace et al., 2020). These clusters are identifiable both in the spectra with peaks around 0.6 Hz and in the cross-correlation analysis, where the associated upward velocities are much higher than predicted by the two-phase theory for slugs. In the dilute zone, the particle fraction evolution with the height exhibits a curved trend, instead of an approximately linear trend in the other regimes. The peak distributions in the spectra are similar in both dense and dilute zones, but the magnitudes are lower in the dilute one.

3. Results and discussions

The control parameters of the experimental setup are the relative pressure in the dispenser, P_{tot}, and the aeration flow rate, $q_{ae}^{\cdot}$. They vary respectively in the ranges 90 – 430 mbar and 0 – 2.5 sm^3/h during all the experiments. The air flow rate range

corresponds to a superficial air velocity in the tube – at the height of the aeration – between 0.01 and 0.54 m/s. Depending on these control parameters, the height of the suspension in the tube – ranging from 0 to H_t – and the particle mass flow rate – ranging from 0 to 392 kg/m^{2}s – are managed. The measured characteristics of the fluidized system are the particle volume fraction and the fluidization regime. The evolutions of the latter are presented in the following section.

3.1. Macroscopic quantities

3.1.1. Height of the suspension

Even if the glass tube enables the visualization of the suspension, it is not always obvious to precisely identify the upper limit of the fluidized bed (without particle circulation), noted H_{bed}, due to the fluctuations of the bed surface. Consequently, the relative pressure profile measured along the tube height is used for a better accuracy. Fig. 2 presents three examples of pressure profile without circulation (circles and triangles), and with particle circulation (squares), each with an aeration flow rate of 0.8 sm^3/h. The pressure decreases linearly, and the height of the suspension is identified at the intersection between the linear regression and the ordinate. With circulation, the relative pressure is necessarily null at the end of the tube, i.e. $H_t = 3.18$ m above the aeration. Based on the experimental data, the method results in a measured height of 3.06 ± 0.13 m, in agreement with the real value of H_t accounting for the measurement uncertainty.

Fig. 3 shows the evolution of the bed height versus the pressure in the dispenser, P_{tot}, without particle circulation, for several values of the aeration flow rate. The bed reaches the level of the injection for a total pressure in the dispenser of approximately 55 – 60 mbar. The trends are then linear for all the tested aeration flow rates (0 – 1.6 sm^3/h). It proves that the hydrostatic pressure of the suspension only contributes to the total pressure drop without particle circulation and that the pressure drop due to wall friction is negligible as explained in (Geldart and Chap, 1986). Furthermore, the particle volume fraction seems to be independent of the bed height, H_{bed}. This point will be discussed in a following section.

3.1.2. Particle mass flow rate

When the suspension reaches the upper tip of the tube, the particles are circulating. The particle mass flux G_p is the particle mass flow rate normalized by the internal tube section, $G_p = \dot{m}_p/S_t$. It varies as a function of both the pressure in the dispenser and the aeration flow rate, as illustrated in Fig. 4. Each point in the Figure corresponds to the mean value over the acquisition period, and the uncertainty bars are calculated as the sum of the measurement uncertainty and the standard deviation of the signal. The latter is relatively low because steady state is reached during the tests, in terms of both pressure and particle mass flow rate variations. As expected, increasing the pressure in the dispenser for a given aeration flow rate or vice versa leads to an increase of the particle mass flux.

At low aeration flow rate, the trends in Fig. 4 are nearly linear, as it was previously observed for relatively low air velocities (Boissiere et al., 2015; Le Gal et al., 2019). Actually, at low values of $\dot{q_{ae}}$, the suspension is dense because the void structures are relatively small and ordered. Then, increasing the pressure leads to the increase of the suspension height without particle circulation. Since the height of the tube is already reached, it corresponds to a linear increase of the particle flow rate. However, an increase of the aeration flow rate results in more disordered void structures that are characteristic of the turbulent and fast fluidization regimes. Then, at low G_p, the particle flow rate is due to the strong fluctuations of the bed surface (in the turbulent fluidization regime), or to the entrainment of particles clusters (in the fast fluidization regimes). Even if the mean suspension has not reached the tube height yet, a slight particle flow is observed. This is the reason why there is no data at these $\dot{q_{ae}}$ values in Fig. 3. When the particle mass flux increases, the trends become more linear because the mean H_{bed} value approaches H_t.

3.1.3. Particle volume fraction

The particle volume fraction α is the ratio of the volume occupied by the particles over the total volume of the gas-particle suspension. According to (Geldart and Chap, 1986), the pressure drop between two pressure probes can be discomposed in three terms.

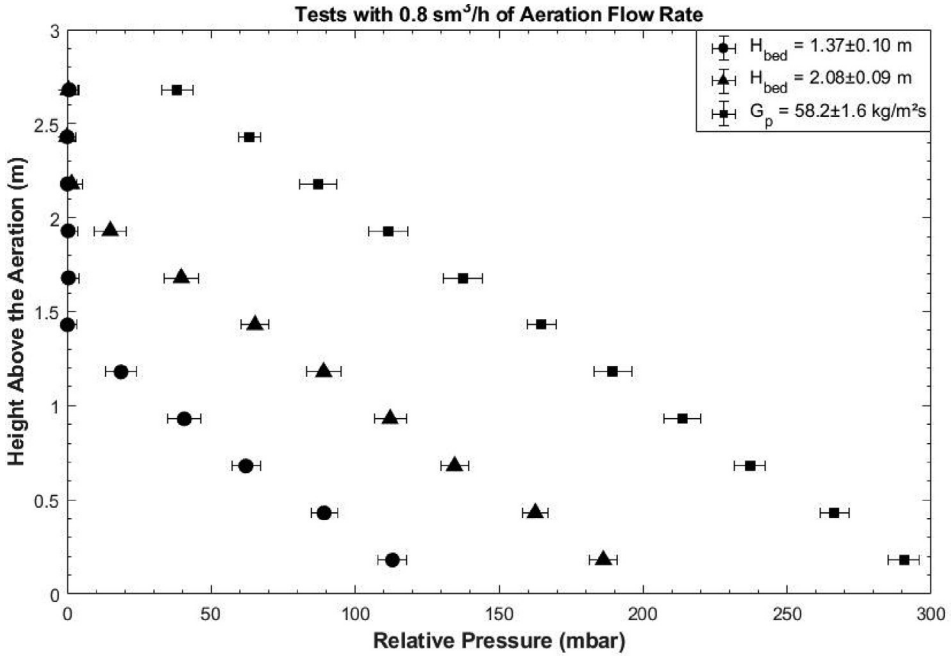

Fig. 2. Typical evolutions of the relative pressure with respect to the height in the tube. Circles and triangles. Without particle circulation, squares. With particle circulation.

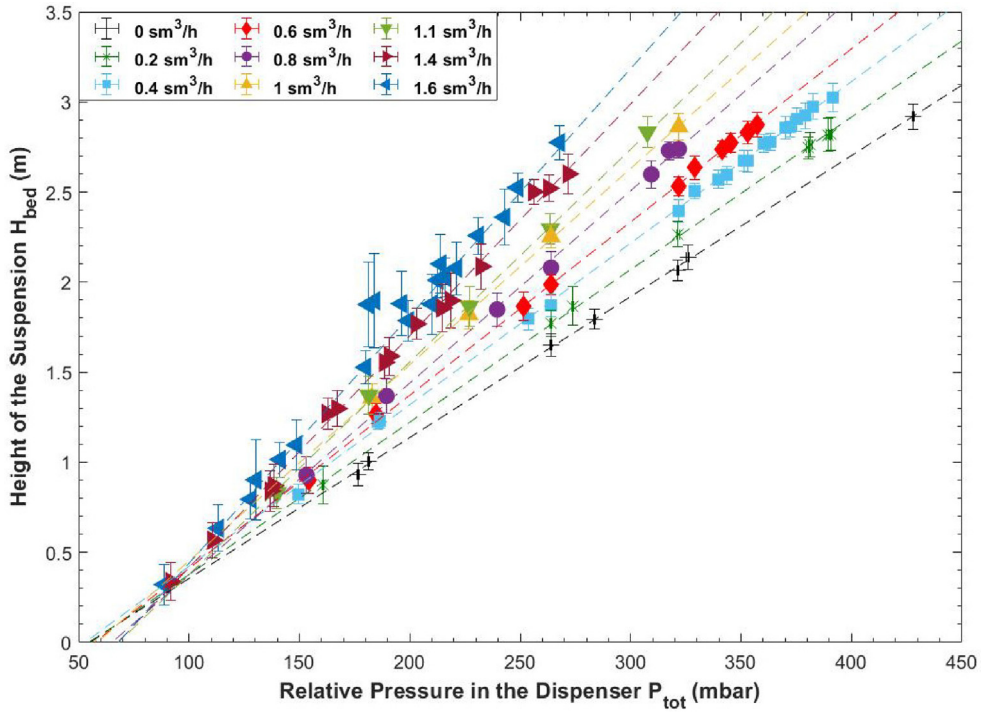

Fig. 3. Evolution of the suspension height versus the pressure in the dispenser for various aeration flow rates. Each symbol corresponds to a given aeration flow rate.

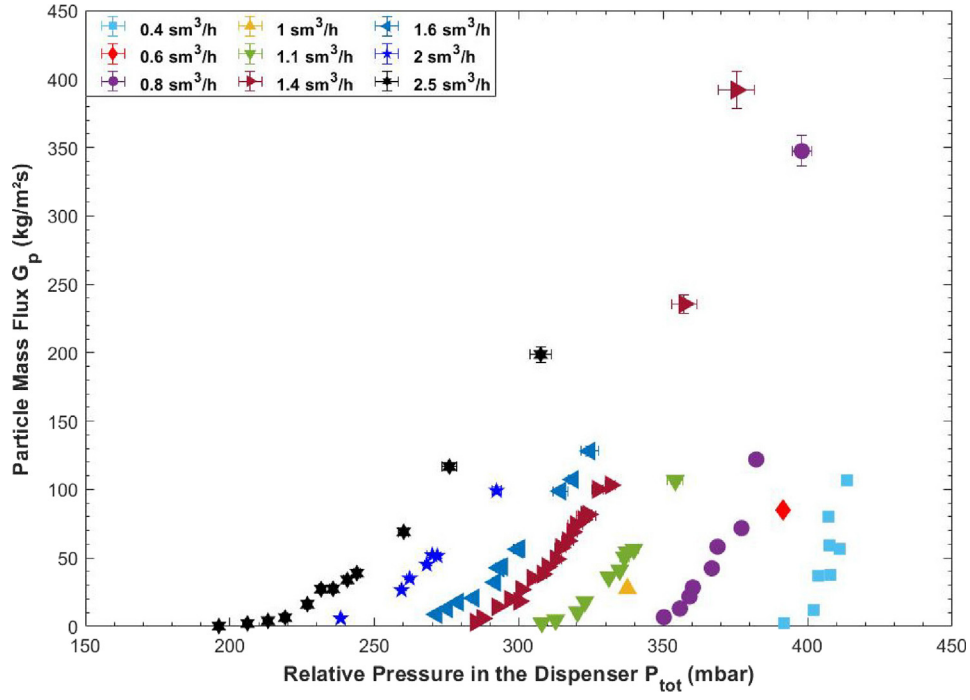

Fig. 4. Evolution of the particle mass flux versus the pressure in the dispenser for various aeration flow rates. Each symbol corresponds to a given aeration flow rate.

A term due to the effective weight of the suspension, a term due to the energy used to accelerate the particle until their upward velocity – proportional to the particle flow rate – and a term due to the friction against the tube walls (Zhang et al., 2017). During all the experiments, the total pressure losses due to particle acceleration and friction represent less than 3 % of the measured pressure drops and are thus neglected. Hence, the local particle volume fraction, noted α_i, can be calculated with Equation (1), with $\overline{\Delta P_i}$ the mean value of the ith differential pressure signal and ΔH the distance between two pressure sockets, i.e. 0.25 m. The associated uncertainty is low due to the low measurement error of the differential pressure sensors, i.e. 0.05 mbar.

$$\alpha_i = \frac{\overline{\Delta P_i}}{\left(\rho_p - \rho_{air}\right) g \Delta H} \tag{1}$$

The evolution of α_i with respect to the height is strongly correlated with the fluidization regime as shown in (Gueguen et al., 2021). A question arising is whether the acquisition time is large enough for the calculation of the particle volume fraction to be representative of the test. To provide an answer a test of one hour has been recorded, without particle circulation and for an aeration flow rate of 0.8 sm^3/h. Fig. 5 plots the evolution of the calculated value of α_i at 1.56 m above the aeration injection as a function of time taken to compute the average value of the differential pressure signal. The horizontal dashed lines represent the value of α_i calculated over all the acquisition duration in black, and the associated uncertainty in red. A minimum acquisition time of around 200 s is needed to converge toward the final value, which is of the order of magnitude of the time needed for the dynamic analysis.

To study the influence of the experimental parameters on the particle volume fraction, an overall value over the bed height is calculated for each test, $\alpha_h = \sum_{i=1}^{N} \alpha_i$. Fig. 6 shows the evolution of the overall particle volume fraction as a function of the suspension height, without circulation. In the Figure, the error bars on α_h and H_{bed} correspond to the pressure and suspension height fluctuations respectively. First, the overall particle fraction is slightly dependent of H_{bed} but decreases with the aeration flow rate. Second, the error bars are stronger for aeration flow rates of 1.4 and 1.6 sm^3/h because such aeration corresponds to the turbulent fluidization regime that is characterized by strong pressure fluctuations.

Fig. 7 presents the evolution of α_h with the particle mass flux G_p, for various aeration flow rates. The increase of the particle volume fraction with the particle mass flow rate, for a given aeration, is due to the acceleration term in the pressure drop balance, $\Delta P_{acc} = G_p/(\rho_p \alpha)$ (Zhang et al., 2017). It means that considering a constant energy given in the system (i.e. the pressure in the dispenser and the aeration flow rate), a part of this energy is consumed to accelerate the particles until their upward velocity. Compared to a case at lower particle velocity – i.e. at lower particle mass flow rate – for a same aeration flow rate, the fraction of total energy used to separate the particle's aggregates decreases at high particle velocity, hence the bed porosity reduces.

Furthermore, one can observe a strong dependency of α_h with the aeration flow rate either for a given particle mass flux or the height of the suspension, as shown in (Gueguen et al., 2021). Actually, the increase of the air velocity is due to the increase of the air flow rate and thus of the air quantity in the tube, which logically results in a quasi-linear decrease of the volume occupied by the particles.

3.2. Fluidization regimes

3.2.1. Diagram of the fluidization regimes

The signal processing described in the previous section have been applied to the 177 tests of the experimental campaign that cover a large range of operating parameters. Fig. 8 presents a diagram of the fluidization regimes identified during this experimental campaign, where 1167 points are plotted, with and without particle circulation. The regimes are identified in the Figure by markers and colors, and plotted in terms of tube height. The height within the tube is normalized with respect to the distance from the aeration nozzle and the internal tube diameter to compare the diagram with the data of previous works on fluidization regimes. Furthermore, according to the scientific literature on circulating fluidized beds, the slip velocity U_{slip} is responsible of the transition between regimes (Rabinovich and Kalman, 2011). The latter is the difference between the interstitial air velocity and the particle velocity (Eq. (2)). It is calculated locally by taking into account of the increase of the local superficial air velocity with height due to the absolute pressure decrease. Actually, considering air as an ideal gas, Equation (3) calculates the superficial air velocity at a given height in the tube, with respect to the superficial air velocity and the pressure at the height of the aeration injection (identified by the subscript $h = 0$). Finally, the points in the diagram are plotted versus the slip velocity expressed as a dimensionless quantity, the local particle Reynolds number (Eq. (4)).

The representation selected for the diagram allows gathering the points in zones corresponding to the same fluidization regime, confirming that the slip velocity is the pertinent parameter that governs the regime transitions. In Fig. 8, the limits between the fluidization regimes are also plotted. The transitions between the different regime zones are discussed in the following paragraphs.

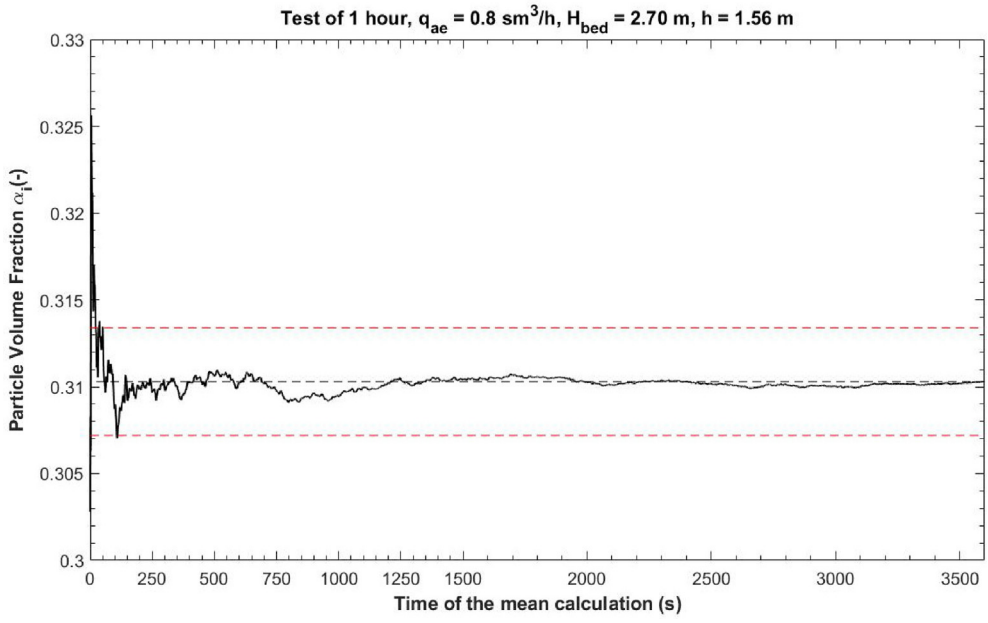

Fig. 5. Evolution of the local particle volume fraction versus the time taken to compute the average differential pressure.

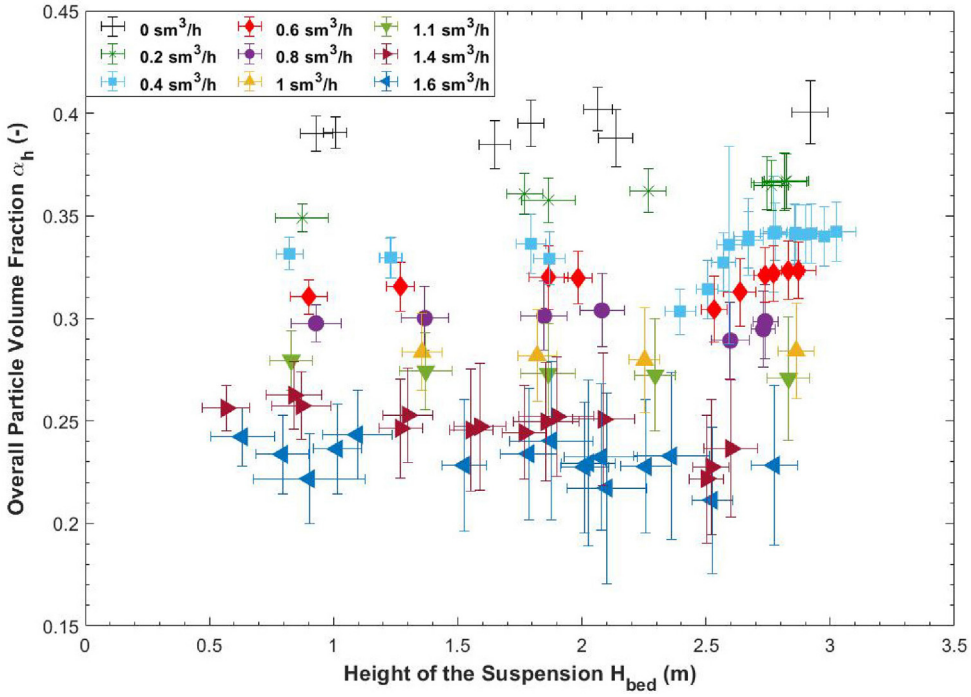

Fig. 6. Evolution of the overall particle volume fraction versus the suspension height for various aeration flow rates. Each symbol corresponds to a given aeration flow rate.

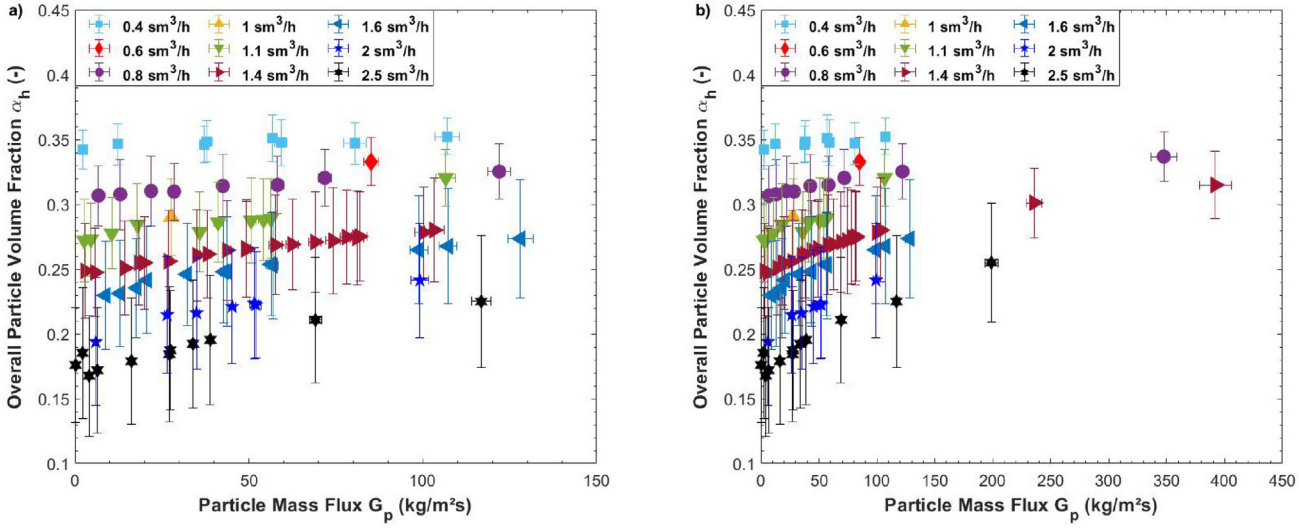

Fig. 7. Evolution of the overall particle volume fraction versus the particle mass flux for various aeration flow rates. Each symbol corresponds to a given aeration flow rate. Fig. 7a is a zoom up to a particle mass flux of 150 kg/(m^{2}s), where a major part of the experimental results is obtained, while the x-axis of Fig. 7b is scaled up to 450 kg/(m^{2}s).

$$U_{slip,i} = \frac{U_{air,i}}{1-\alpha_i} - \frac{G_p}{\rho_p \alpha_i} \tag{2}$$

$$U_{air,i} = \frac{U_{air,h=0} P_{h=0}}{P_i} \tag{3}$$

$$Re_{slip} = \frac{\rho_{air} U_{slip} d_{SV}}{\mu_{air}} \tag{4}$$

Compared to the previous experimental works on the fluidized particle-in-tube receiver concept (Flamant et al., 2013; Benoit et al., 2015; Perez-Lopez et al., 2016; Boissiere et al., 2015; Le Gal et al., 2019; Ansart et al., 2017; Benoit et al., 2018; Kong et al., 2017; Sabatier et al., 2020; Deng et al., 2021), this diagram highlights the turbulent and fast fluidization regimes at high slip velocities. Along the tube height, the turbulent fluidization zone (black circles in the Figure) is preceded by a bubbling zone until approximately dimensionless height of 10 above the aeration, where the bubbles are splitting instead of coalescing, as previously observed (Gueguen et al., 2021). Actually, according to (Grace et al., 2020), the transition velocity from bubbling to turbulent regimes for fine particles can be predicted by assuming the existence of a maximum stable bubble size. Trailing bubbles split in the turbulent wake of leading bubbles. A leading bubble of maximum stable size induces the break of a trailing bubble into small voids by interaction with its turbulent wake. Consequently, when bubble splitting becomes dominant, the massive breakdown of bubbles transforms the flow from bubbling to turbulent fluidization. To simplify the

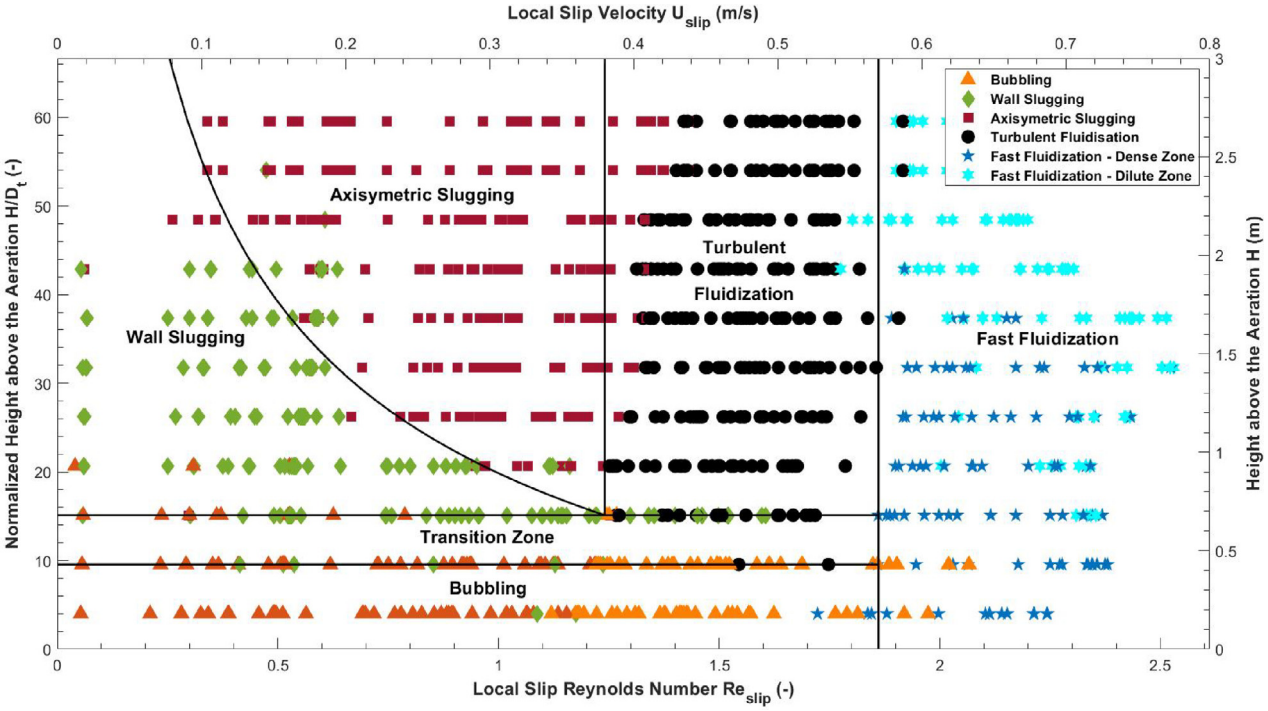

Fig. 8. Diagram of the fluidization regimes encountered in the tube and their transitions with the height as a function of the experimental parameters expressed in terms of dimensionless quantities.

diagram, vertical limits are considered and calculated to maximize the number of points corresponding to the regimes in the associated zones. The limits of regimes are obtained with 233 points identified as in turbulent fluidization regime in the related zone among a total of 269 points, and 200 points identified as fast fluidization regime over 209 points in their corresponding zone. The velocity limits for U_t and U_k are 0.38 and 0.57 m/s respectively, i.e. particle Reynolds numbers of 1.24 and 1.86 respectively. Moreover, it seems that the turbulent fluidization occurs when the wall slugging zone disappears (in green in the Figure). This finding is in good agreement with the interpretation that the bubble's coalescence becomes negligible compared to their scission at the onset of the turbulent fluidization regime, as proposed by (Bi et al., 2000). Limit of the wall slugging zone is discussed below.

The points identified as in bubbling regime below the turbulent and fast fluidization zones slightly differ from those related to the classical single bubbling regime (they are represented in the Figure with triangles lighter than those corresponding to the classical bubbling). Actually, their spectra present the classical peak distribution above 1 Hz but also some peak distributions below 1 Hz, even if the latter have very low magnitudes, too low to be considered as indicators of turbulent or fast fluidization. This may be due to the retroaction of strong fluctuations occurring at higher locations in the tube but also to the influence of the aeration injection. Indeed, given the air flow rates injected through the small diameter injection, between 0 and 2.5 sm^3/h, the corresponding horizontal air velocity ranges between 0 and 480 m/s ($0 \leq Re \leq 38\,200$). According to (Wang et al., 2015), the length of the penetration jet is increasing with the increase of $\dot{q_{ae}}$, with approximately $2D_t$ for an aeration flow rate of 2.5 sm^3/h. Furthermore, penetration jets are associated to various upward angles that decrease with the increase of the air flow rate. For an aeration of 2.5 sm^3/h, this angle θ is estimated at 10°. A simple calculation allows to estimate the height of the corresponding jet in the vertical main tube, $D_t/\sin\theta$, of 0.26 m, i.e. above the first pressure sensor. As a conclusion, strong perturbations are induced in the aeration nozzle zone that results in a dissipation height spreading until the firsts pressure sensors. Numerical simulations are under progress to study this phenomenon and complete this interpretation.

There is a slight zone between the second and the third pressure sockets, i.e. between approximately 10 and 15 of dimensionless heights above the aeration, where all three bubbling, wall slugging and turbulent fluidization regimes are identified depending on the operation conditions. This zone is named "Transition Zone" to take into account the identification uncertainties. Then, below this transition zone 97 points are identified as in bubbling regime over 102 points.

As explained above in the paper, in a bubbling/slugging operation conditions, the bubbles are progressively merging into slugs (Sabatier et al., 2020). In the diagram, at approximately a dimensionless height of 10 above the aeration, bubbles start to coalesce into an intermediate wall-slugging zone. The wall-slugging zone appears to be thinner and thinner with the increase of the slip velocity. This observation differs with previous published works, where the wall slugging to the axisymmetric slugging transition was identified at a constant height (Kong et al., 2017; Sabatier et al., 2020; Deng et al., 2021). Regarding the bubbles coalescence, the reference study (Mori and Wen, 1975) proposed an empirical correlation for the evolution of the bubble diameter with height for group B particles as a function of the air velocity. Considering the diameter at which the bubbles are coalescing into slugs, i.e. around 60 % of the tube diameter (Geldart, 1986), the equation can be reworked in order to determine the height of the slug transition, here noted h_s, as a function of the slip velocity to take into account the particle circulation. The general trend is given by Equation (5), with the coefficients A, B and C determined for group B particles in the initial empirical correlation (Mori and Wen, 1975). To determine these coefficients in the case of group A particles, we assume the following. Since the minimum bubbling velocity is defined as the air velocity at which the first bubble is erupting at the bed surface (Abrahamsen and Geldart, 1980), the transition height for the coalescence of the same bubble into a slug

at this velocity can be mathematically considered at the infinite. In Equation (5), it happens when the term in the logarithm becomes null. Then, considering $U_{slip} = U_{mb}$, it gives $C = BU_{mb}^{0,4}$. Furthermore, a given point of the correlation can be identified at the beginning of the turbulent fluidization regime, i.e. at $U_{slip} = 0.38$ m/s and a height of approximately 0.7 m (i.e. respectively at $Re_{slip} = 1.24$ and $H/D_t = 15$), fixing the A coefficient as a function of B. Several values of the B coefficient have been numerically tested, and it has been determined by maximizing both the ratio of the points identified as wall slugs over the total points in the wall slugging zone (below the transition), and the ratio of the points identified as axisymmetric slugs over the total points in the axisymmetric slugging zone (above the transition). The best fit has been established for the following coefficients: $A = 227.168$, $B = 1.15$ and $C = 0.1456$. A total of 126 points have been identified as in wall-slugging regime among 157 points in the associated zone, and 216 points have been identified as in axisymmetric slugging regime among 229 points in the corresponding zone.

It comes, height of the slug transition,

$$h_s = -A \ln\left(B - \frac{C}{U_{slip}^{0.4}}\right) \tag{5}$$

With $A = 227.168$, $B = 1.15$ and $C = 0.1456$.

Finally, combining all the limits presented above, it gives 872 points well-identified in their corresponding fluidization regime zones over a total of 966 points, i.e. a validation of the transition limits of 90.26 %.

For the sake of clarity, Fig. 9 illustrates the diagram of the fluidization regimes without any experimental points but only with the transitions between the fluidization regimes, considering a relative uncertainty of 10 %. Actually, the relative uncertainties due to measurement related to the local slip velocities are between 5 and 7 %. Then, four transition zones appear in the simplified diagram of Fig. 9 (in gray), delimiting the regimes zones of bubbling, wall slugging, axisymmetric slugging, turbulent fluidization, and fast fluidization.

Obtaining a complete diagram of the fluidization regimes is one of the major issues in the fluidization domain. As the regime transitions depend on the particle properties, some authors have established diagrams in terms of Archimedes' number to compare the various Geldart groups of particles (Geldart, 1973), as Bi & Grace (Grace et al., 2020; Rabinovich and Kalman, 2011; Geldart and Chap, 1986; Bi and Grace, 1995) and more recently Rabinovitch and Kalman (Rabinovich and Kalman, 2011). In these diagrams, the air velocity and the tube geometry are gathered in the Reynolds' number. Nevertheless, these widely used diagrams are related to circulating fluidized beds inside risers. Consequently, the limits of the turbulent and fast fluidization regimes differ significantly with our experimental values that are much lower than the established correlations, even considering the large uncertainties associated with correlations (around 30 %) (Ellis et al., 2004). The results indicate turbulent and fast fluidization transition velocities from 1.3 to 2.4 times lower than literature correlations. Two main explanations arise. First, the correlations are based the Sauter diameter, while the powder used in this study is characterized by a rather large particle size distribution with a non-negligible amount of fine particles that can modify the fluidization properties. Second, the pressure is a control parameter of our system. Actually, pressurizing the system rises the particle energy level. As a result, the energy share – associated to the air phase – required to induce the regime transition is lower than the one observed in risers. Consequently, a general criterion or correlation cannot gather the two kinds of concept – risers and pressure-driven fluidized particle-in-tube – for the moment.

3.2.2. Discussion on the detection criteria

Fig. 10 presents the measured local solid volume fraction, α_i, in terms of the local slip Reynolds number $Re_{slip,i}$, calculated at the same height, over all the tests. The experimental points and their associated regimes are the same that in Fig. 8. They gather in a linear trend, independently of the aeration and the particle mass flow rates, with and without particle circulation. The limits of the fluidization regimes are identified in the Figure with the transition

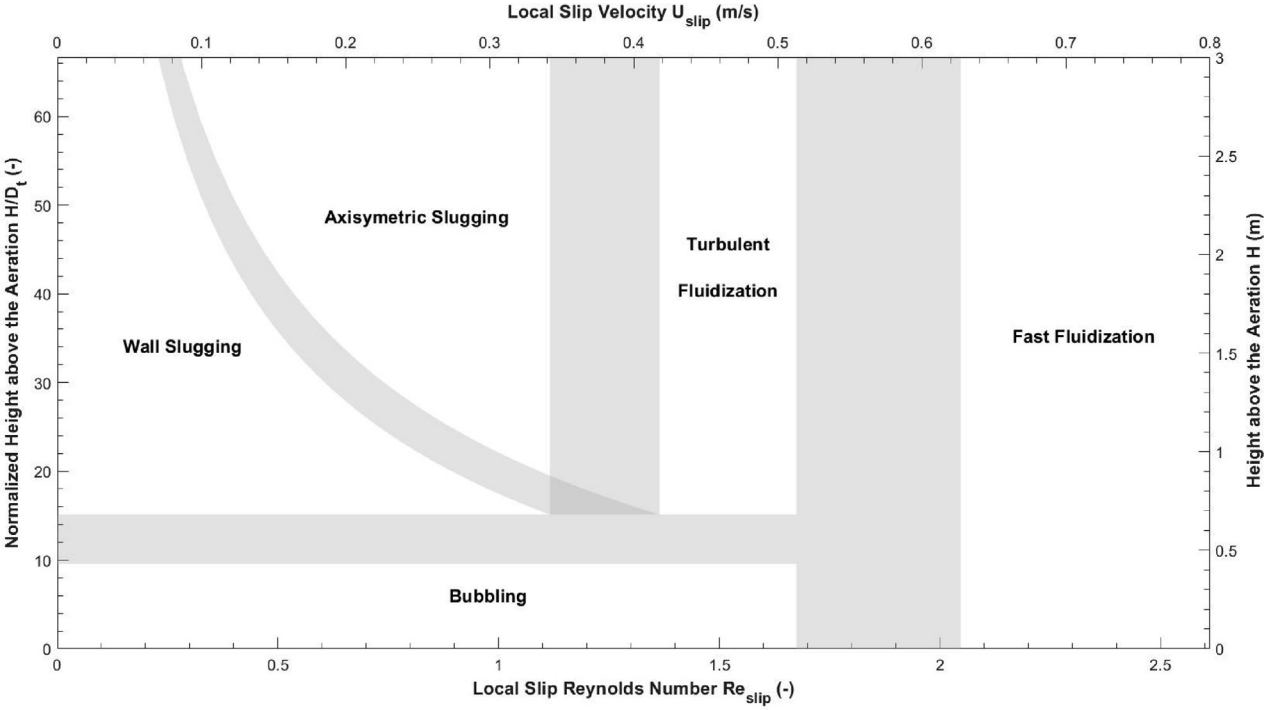

Fig. 9. Simplified diagram of the fluidization regimes with transition zones established with a trust interval of 90 %.

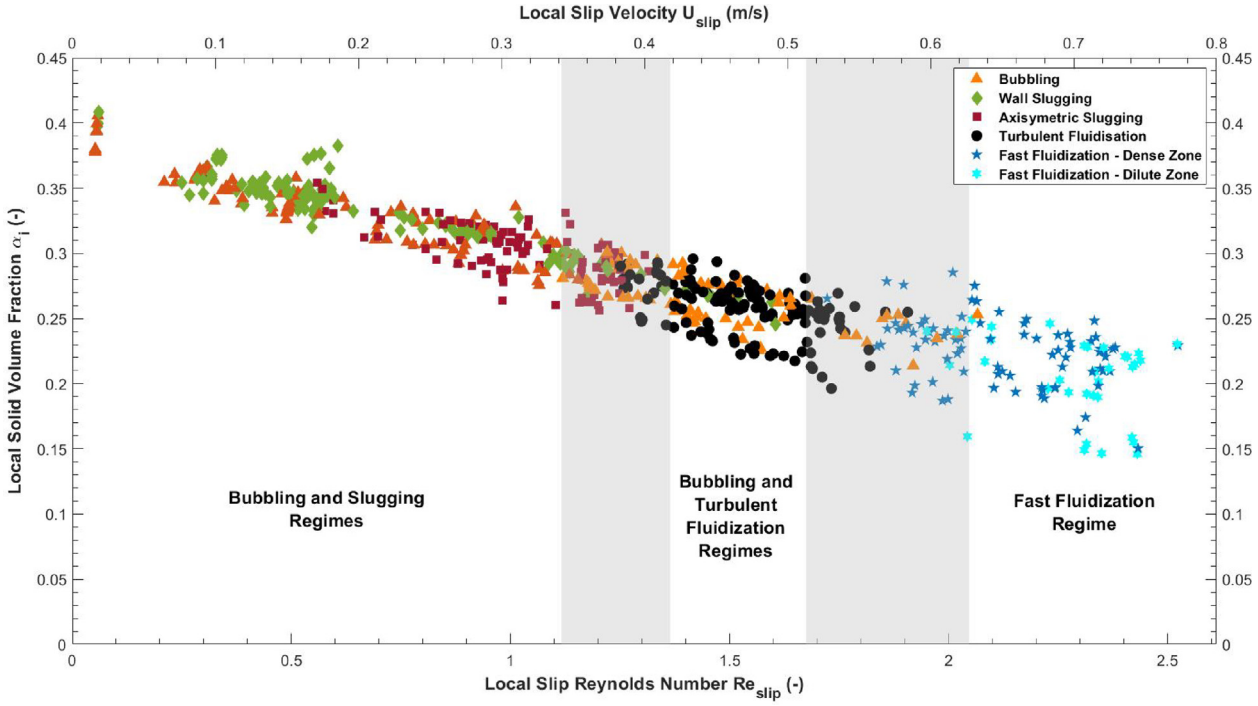

Fig. 10. Evolution of the local particle volume fraction with the local slip Reynolds number.

zones of Fig. 8. Values of the particle volume fraction can thus be associated to these regimes as presented in Table 2. The range of the particle volume fraction corresponding to the turbulent fluidization regime, i.e. between 0.21 and 0.29, is in good agreement with the two-phase theory that predicts a value of 0.275 (Grace et al., 2020).

Then, simple calculation of the particle volume fraction at a given height and local slip velocity allow identifying the fluidization regimes. This simple method prevents heavy dynamic analyses of the pressure signals.

Since the local slip velocity is the governing parameters of the fluidization regimes, it is relevant to discuss the evolution of the local relative pressure fluctuations – i.e. the ratio of the standard deviation of a differential pressure signal by its mean value – versus the local slip Reynolds number. The results indicate that the local relative pressure fluctuations increase with this number. Accounting for the decrease of the local volume fraction with the local slip Reynolds number (Fig. 10), Fig. 11 represents the relationship between the pressure fluctuation and the particle volume fraction. Interestingly, the two parameters are correlated, and the trend is a negative exponential curve. In addition, Fig. 11 shows that the bubbling regime exhibits a different trend than the others fluidization regimes.

Table 2
Ranges of local slip Reynolds numbers and particle volume fractions associated to the fluidization regimes configurations.

Fluidization Regimes	Dimensionless Transition Height, H/D_t	Local Particle Volume Fraction, α_i	Local Slip Reynolds Number, Re_{slip}
Bubbling and Slugging	10 – 15	0.26 – 0.41	0 – 1.12
Bubbling and Turbulent Fluidization	10 – 15	0.21 – 0.29	1.37 – 1.67
Fast Fluidization (Dense and Dilute Zones)	Varying	0.14 – 0.27	2.05 – 2.53

4. Conclusions

The behavior of upward gas-particle fluidized beds has been studied in a tube with a large aspect ratio at ambient temperature, for application as heat transfer fluid in a tubular particle solar receiver. The selected particles are Geldart group A olivine, the superficial air velocity ranges between 0.01 and 0.54 m/s, and the particle mass flux varies from 0 to 390 kg/(m^2.s).

Experimental results show that the particle volume fraction α varies slightly with the height of the suspension without particle circulation. With particle circulation, it increases with the particle mass flux due to supplementary pressure drop terms. Moreover, at a given height or particle flow rate, α decreases strongly and quasi linearly with the superficial air velocity.

The fluidization regimes are driving the particle mixing and thus the heat transfer between the tube walls and the particles. Bubbling, slugging (wall and axisymmetric), turbulent fluidization and fast fluidization regimes have been identified in the tube depending on the experimental conditions using pressure signals processing methods.

A complete diagram of the fluidization regimes has been established by considering the height in the tube versus the local slip velocity, ranging from 0.01 to 0.78 m/s. It proves that, even for a pressure-assisted system, the slip velocity is the pertinent parameter that governs the flow structure. It is shown that at low slip velocities, bubbles are present at the bottom of the tube and coalesce with the height into axisymmetric slugs when the bubble size (D_b) is comparable to the tube diameter (D_t), with $D_b/D_t > 0.6$. The intermediate zone between bubbles and axisymmetric slugs is a coalescence zone, where wall slugs are present. This zone shrinks with the increase in the slip velocity, as it can be verified by applying a simple coalescence correlation. At higher slip velocity, the interaction of the maximum bubble size wake with the following bubbles results in the splitting of the latter in small voids. In other words, the split of the bubbles exceeds the coalescence, leading to the turbulent fluidization regime. At higher velocity, bubbles disappear and the gas solid flow structure is dominated by particle

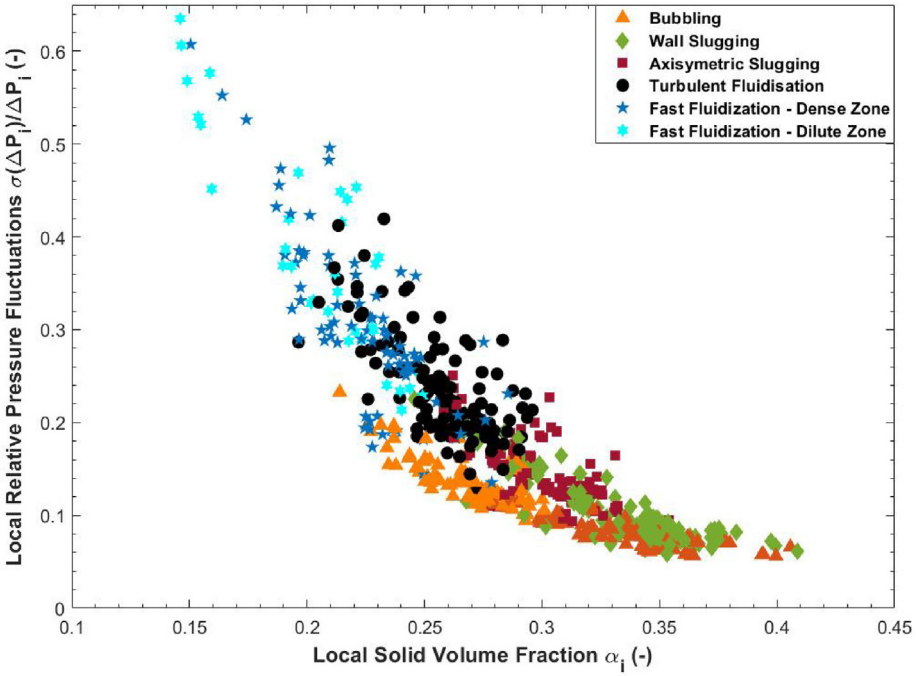

Fig. 11. Evolution of the local relative pressure fluctuations with the local particle volume fraction.

aggregates, the clusters, representative of the fast fluidization regime.

The following observations arise from the analysis of the pressure signal processing. Starting with the bubbling and slugging regime zone at low velocity and increasing the slip velocity leads to a decrease of the dominant frequency and an increase of the associated magnitude in the power spectra. Both the relative pressure fluctuations and the velocity measured with the cross-correlation method increase, while the local particle volume fraction decreases. Furthermore, increasing the slip velocity leads both to a decrease of the local particle volume fraction and an increase of the local relative pressure fluctuations, these two parameters being strongly correlated. The main shortcomings of the regimes' identification method based on the analysis of temporal pressure signals are its weak precision and inability to measure the special distribution of the detected structures. It was selected since it is applicable at high temperature under on-sun operation, which is the targeted application.

According to the literature data related to risers, the turbulent fluidization regime is the best compromise in terms of heat transfer because it is associated with a strong particle mixing and a rather dense suspension, hence it should be preferred in wall-heating conditions of tubes. The limits of the turbulent fluidization regime have been measured for a local slip velocity between 0.42 and 0.51 m/s, corresponding to particle Reynolds number of 1.37 and 1.67. Furthermore, it appears that the particle volume fraction (α) decreases linearly with the slip velocity. The corresponding limits for the turbulent fluidization regime are 0.29 – 0.21. Finally, the knowledge of the particle volume fraction at a known height – thanks to pressure drop measurement may be sufficient to identify the fluidization regimes in the tube, if the acquisition time is sufficient.

Considering concentrating solar thermal applications, the question of influence of temperature on the fluidization regimes and their transitions is a key issue. Experiments under concentrated solar power using a refractory alloy receiver tube are in progress to answer this question and measure the associated wall-to-bed heat transfer coefficients.

CRediT authorship contribution statement

Ronny Gueguen: Investigation, Methodology, Data curation, Writing – original draft, Writing – review & editing. **Guillaume Sahuquet:** Investigation, Methodology, Data curation, Writing – original draft, Writing – review & editing. **Samuel Mer:** Validation, Data curation, Writing - review & editing. **Adrien Toutant:** Validation, Data Curation, Visualization, Writing – review & editing. **Françoise Bataille:** Validation, Data Curation, Visualization, Writing – review & editing. **Gilles Flamant:** Investigation, Methodology, Data curation, Writing – original draft, Writing – review & editing, Supervision, Project administration, Funding acquisition.

Data availability

Data will be made available on request.

Declaration of Competing Interest

The authors declare that they have no known competing financial interests or personal relationships that could have appeared to influence the work reported in this paper.

Acknowledgements

The characterization of the olivine sample was conducted with the help of the Material Characterization Platform – Surfaces and Interfaces Analyses of the PROMES (CNRS) laboratory.

Funding

This work was funded by the French "Investments for the future" ("*Investissements d'Avenir*") program managed by the National Agency for Research (ANR) under contract ANR-10-

LABX-22-01 (labex SOLSTICE). Additional funding was awarded by the European Union's Horizon 2020 research and innovation program under Grant Agreement 727762, Next-CSP project. Additional funding was obtained by the Occitanie French region for the cold mock-up installation.

References

Abrahamsen, A.R., Geldart, D., 1980. Behaviour of Gas-Fluidized Beds of Fine Powders Part I. Homogeneous Expansion. Powder Technol. 26, 35–46. https://doi.org/10.1016/0032-5910(80)85005-4.

Ansart, R., Garcia-Triñanes, P., Boissière, B., Benoit, H., Seville, J.P.K., Simonin, O., 2017. Dense gas-particle suspension upward flow used as heat transfer fluid in solar receiver: PEPT experiments and 3D numerical simulations. Powder Technol. 307, 25–36. https://doi.org/10.1016/j.powtec.2016.11.006.

Benoit, H., Perez Lopez, I., Gauthier, D., Sans, J.L., Flamant, G., 2015. On-sun demonstration of a 750 °C heat transfer fluid for concentrating solar systems: Dense particle suspension in tube. Solar Energy 118, 622–633. https://doi.org/10.1016/j.solener.2015.06.007.

Benoit, H., Spreafico, L., Gauthier, D., Flamant, G., 2016. Review of heat transfer fluids in tube-receivers used in concentrating solar thermal systems: Properties and heat transfer coefficients. Renewable Sustainable Energy Rev. 55, 298–315. https://doi.org/10.1016/j.rser.2015.10.059.

Benoit, H., Ansart, R., Neau, H., Garcia Triñanes, P., Flamant, G., Simonin, O., 2018. 3D numerical simulation of upflow bubbling fluidized bed in opaque tube under high flux solar heating. Am. Inst. Chem. Eng. J. 64. https://doi.org/10.1002/aic.16218.

Bi, H.T., Grace, J.R., Zhu, J.X., 1993. Types of Chocking in Vertical Pneumatic Systems. Int. J. Multiph. Flow 19, 1077–1092. https://doi.org/10.1016/0301-9322(93)90079-A.

Bi, H.T., Grace, J.R., 1995. Flow regime diagrams for gas-solid fluidization and upward transport. Int. J. Multiph. Flow 21, 1229–1236. https://doi.org/10.1016/0301-9322(95)00037-X.

Bi, H.T., Ellis, N., Abba, I.A., Grace, J.R., 2000. A state-of-the-art review of gas-solid turbulent fluidization. Chem. Eng. Sci. 55, 4789–4825. https://doi.org/10.1016/S0009-2509(00)00107-X.

Boissiere, B., Ansart, R., Gauthier, D., Flamant, G., Hemati, M., 2015. Experimental Hydrodynamic Study of Gas-Particle Dense Suspension Upward Flow for Application as New Heat Transfer and Storage Fluid. Can. J. Chem. Eng. 93 (2), 317–330.

Breault, R.W., Weber, J., Shadle, L.J., 2020. The development of a generalized riser flow regime map based upon higher moment and chaotic statistics using electrical capacitance volume tomography (ECVT). Power Technol. 365, 12–27. https://doi.org/10.1016/j.powtec.2019.03.036.

Chen, Y., Lim, C.J., Grace, J.R., Zhang, J., Zhao, Y., Zheng, C., 2015. Characterization of pressure fluctuations from a gas-solid fluidized bed by structure density function analysis. Chem. Eng. Sci. 129, 156–167. https://doi.org/10.1016/j.ces.2015.02.009.

Deng, Y., Sabatier, F., Dewil, R., Flamant, G., Le Gal, A., Gueguen, R., Baeyens, J., Li, S., Ansart, R., 2021. Dense upflow fluidized bed (DUFB) solar receivers of high aspect ratio: Different fluidization modes through inserting bubble rupture promoters. Chem. Eng. J. 418,. https://doi.org/10.1016/j.cej.2021.129376 129376.

Dodds, J., Baluais, G., 1993. Particle size characterization. Sci. Géol. 46, 79–104. https://doi.org/10.3406/sgeol.1993.1898.

Dunham, M.T., Iverson, B.D., 2014. High-efficiency thermodynamic power cycles for concentrated solar power systems. Renew. Sustain. Energy Rev. 30, 758–770. https://doi.org/10.1016/j.rser.2013.11.010.

Ellis, N., Bi, H.T., Lim, C.J., Grace, J.R., 2004. Hydrodynamics of turbulent fluidized beds of different diameters. Powder Technol. 141, 124–136. https://doi.org/10.1016/j.powtec.2004.03.001.

Fan, L.T., Ho, T.C., Walawender, W.P., 1983. Measurements of the Rise Velocities of Bubbles, Slugs and Pressure Waves in a Gas-Solid Fluidized Bed Using Pressure Fluctuation Signals. American Inst. Chem. Eng. J. 29, 33–39. https://doi.org/10.1002/aic.690290105.

CSP2 (2015). Dense suspensions of solid particles as a new heat transfer fluid for CSP. https://cordis.europa.eu/project/id/282932 (accessed on 6 May 2022).

G. Flamant, H. Hemati, Dispositif Collecteur D'énergie Solaire (Device for Collecting Solar Energy), French Patent FR 1058565, 20 October 2010; PCT extension WO2012052661, 26 April 2012.

Flamant, G., Gauthier, D., Benoit, H., Sans, J.L., Garcia, R., Boissière, B., Ansart, R., Hemati, M., 2013. Dense suspension of solid particles as a new heat transfer fluid for concentrated solar thermal plants: On-sun proof of concept. Chem. Eng. Sci. 102, 567–576. https://doi.org/10.1016/j.ces.2013.08.051.

Geldart, D., 1973. Types of Gas Fluidization. Powder Technol. 7, 285–292. https://doi.org/10.1016/0032-5910(73)80037-3.

Geldart, D., 1986. Chap.2: Single particles, Fixed and Quiescent Beds. In Gas Fluidization Technology, pp. 11–32.

Geldart, D., 1986. Chap.4: Hydrodynamics of Bubbling Fluidized Beds. In Gas Fluidization Technology, pp. 53–96.

Geldart, D., 1986. Chap. 6: Particle Entrainment and Carryover. In Gas Fluidization Technology, 123–154.

Grace, J.R., Bi, X., Ellis, N., 2020. Chap. 4: Gas Fluidization Flow Regimes. In Essential of Fluidization Technology, 55–74.

Grace, J.R., Bi, X., Ellis, N., 2020. Chap. 9: Turbulent Fluidization. In Essential of Fluidization Technology, 163–180.

Gueguen, R., Grange, B., Bataille, F., Mer, S., Flamant, G., 2020. Shaping High Efficiency, High Temperature Cavity Tubular Solar Receivers. Energies 13, 4803. 10.3390.en13184803.

Gueguen, R., Sahuquet, G., Mer, S., Toutant, A., Bataille, F., Flamant, G., 2021. Gas-Solid Flow in a Fluidized-Particle Tubular Solar Receiver: Off-Sun Experimental Flow Regimes Characterization. Energies 14, 7392. https://doi.org/10.3390/en14217392.

Hafizur Rahman, M., Bi, X.T., Grace, J.R., Jim Lim, C., 2020. Comparison of techniques for measuring CFB solids circulation rates at low and high temperatures. Powder Technol. 360, 43–54. https://doi.org/10.1016/j.powtec.2019.10.033.

Ho, C.K., Christian, J., Yellowhair, J., Jeter, S., Golob, M., Nguyen, C., Repole, K., Abdel-Khalik, S., Siegel, N., Al-Ansary, H., El-Leathy, A., Gobereit, B., 2017. Highlights of the high-temperature falling particle receiver project: 2012–2016. AIP Conference Proceeding 1850,. https://doi.org/10.1063/1.4984370 030027.

Jacob, R., Belusko, M., Ines Fernandez, A., Cabeza, L.F., Saman, W., Bruno, F., 2016. Embodied energy and cost of high temperature thermal energy storage systems for use with concentrated solar power plants. Appl. Energy 180, 586–597. https://doi.org/10.1016/j.apenergy.2016.08.027.

Johnsson, F., Zijerveld, R.C., Schouten, J.C., van den Bleek, C.M., Leckner, B., 2000. Characterization of fluidization regimes by time-series analysis of pressure fluctuations. Int. J. Multiph. Flow 26, 663–715. https://doi.org/10.1016/S0301-9322(99)00028-2.

Kang, Q., Flamant, G., Dewil, R., Baeyens, J., Zhang, H.L., Deng, Y., 2019. Particles in a circulation loop for solar energy capture and storage. Particuology 43, 149–156. https://doi.org/10.1016/j.partic.2018.01.009.

Kong, W., Tan, T., Baeyens, J., Flamant, G., Zhang, H., 2017. Bubbling and slugging of Geldart group A powders in small diameters columns. Ind. Eng. Chem. Res. 56, 4136–4144. https://doi.org/10.1021/acs.iecr.6b04798.

Kunii, D., Levenspiel, O., 1991. Chap 3: Fluidization and Mapping of Regimes. In Fluidization Eng., 61–94

Le Gal, A., Grange, B., Tessonneaud, M., Perez, A., Escape, C., Sans, J.L., Flamant, G., 2019. Thermal analysis of fluidized particle flows in a finned tube solar receiver. Sol. Energy 191, 19–33.

Li, Y.-Q., Grace, J.R., Gopaluni, R.B., Bi, H., Lim, C.J., Ellis, N., 2011. Characterization of gas-solid fluidization: A comparative study of acoustic and pressure signals. Powder Technol. 214 (2), 200–210.

Mori, S., Wen, Y., 1975. Estimation of Bubble Diameter in Gaseous Fluidized Beds. Am. Inst. Chem. Eng. J. 21, 109–115. https://doi.org/10.1002/aic.690210114.

Next-CSP, 2020. High Temperature Concentrated Solar Thermal Power Plant with Particle Receiver and Direct Thermal Storage. https://cordis.europa.eu/project/id/727762 (accessed on 10 March 2022).

Perez-Lopez, I., Benoit, H., Gauthier, D., Sans, J.L., Guillot, E., Mazza, G., Flamant, G., 2016. On-sun operation of a 150 kW_{th} pilot solar receiver using dense particle suspension as heat transfer fluid. Sol. Energy 137, 463–476. https://doi.org/10.1016/j.solener.2016.08.034.

Rabinovich, E., Kalman, H., 2011. Flow regime diagram for vertical pneumatic conveying and fluidized bed systems. Powder Technol. 207, 119–133. https://doi.org/10.1016/j.powtec.2010.10.017.

Sabatier, F., Ansart, R., Zhang, H., Baeyens, J., Simonin, O., 2020. Experiments support simulations by NEPTUNE CFD Code in a Upflow Bubbling Fluidized Bed reactor. Chem. Eng. J. 385,. https://doi.org/10.1016/j.cej.2019.123568 123568.

Stefanova, A., Bi, H.T., Lim, J.C., Grace, J.R., 2011. Local hydrodynamics and heat transfer in fluidized beds of different diameter. Powder Technol. 212, 57–63. https://doi.org/10.1016/j.powtec.2011.04.026.

Stefanova, A., Bi, H.T., Lim, C.J., Grace, J.R., 2020. A probabilistic heat transfer model for turbulent fluidized beds. Powder Technol. 365, 163–171. https://doi.org/10.1016/j.powtec.2019.01.066.

Vaidheeswaran, A., Li, C., Ashfaq, H., Wu, X., Rowan, S., Rogers, W.A., 2022. Validation experiments on bubbling fluidization of Group B glass particles. Exp. Comput. Multiphase Flow 4, 264–273. https://doi.org/10.1007/s42757-021-0108-4.

van der Schaaf, J., Schouten, J.C., Johnsson, F., van den Bleek, C.M., 2002. Non-intrusive determination of bubble and slug length scales in fluidized beds by decomposition of the power spectral density of pressure time series. Int. J. Multiph. Flow 28 (5), 865–880.

Wang, S., Yang, Q., Shao, B., Zhao, J., Liu, L., Liu, Y., 2015. Numerical Simulation of Horizontal Jet Penetration Using Filtered Fluid Model in Gas-Solid Fluidized Bed. Powder Technol. 276, 1–9. https://doi.org/10.1016/j.powtec.2015.02.009.

Wu, W., Amsbeck, L., Buck, R., Uhlig, R., Ritz-Paal, R., 2014. Proof of concept test of a centrifugal particle receiver. Energy Proc. 49, 560–568. https://doi.org/10.1016/j.egypro.2014.03.060.

Wu, S.Y., Baeyens, J., 1991. Effect of operating temperature on minimum fluidization velocity. Powder Technol. 67, 217–220. https://doi.org/10.1016/0032-5910(91)80158-F.

Yerushalmi, J., Cankurt, N.T., 1979. Further studies of the regimes of fluidization. Powder Technol. 24, 187–205. https://doi.org/10.1016/0032-5910(79)87036-9.

Zhang, H., Kong, W., Tan, T., Baeyens, J., 2017. High-efficiency concentrated solar power plants need appropriate materials for high-temperature heat capture, conveying and storage. Energy 139, 52–64. https://doi.org/10.1016/j.energy.2017.07.129.

Zhang, H., Kong, W., Tan, T., Flamant, G., Baeyens, J., 2017. Experiments support an improved model for particle transport in fluidized beds. Sci. Rep. 7, 10178. https://doi.org/10.1038/s41598-017-10597-3.